

## Supporting Information

### **Mechanistic Understanding of the Thermal-Assisted Photocatalytic Oxidation of Methanol-to-Formaldehyde with Water Vapor over Pt/SrTiO<sub>3</sub>**

*Michel Deitermann, Takuma Sato, Yannik Haver, Alexander Schnegg, Martin Muhler and Bastian Timo Mei\**

For catalytic testing, the photocatalyst was applied onto a heated (200 °C) sand-blasted quartz glass plate (100 mm x 150 mm) via spray coating using a custom-made set-up. The suspension of the catalyst in isopropanol (99.8 %, Fisher Chemical) was pumped with a syringe pump (Cavro Xcalibur Tecan, SETonic syringes, 100 µL) to the glass nozzle where it was dispersed with compressed air. To avoid sedimentation, the suspension was ultrasonicated (45 min, Bandelin electronic DK 514 BP) and manually mixed every 15 min before and stirred during the spray-coating process. The standard catalyst area of 60 mm x 100 mm was achieved by covering parts of the quartz glass plate with aluminum foil which therefore remained uncoated. The syringe pump speed, volume and position of the glass nozzle in x- and y- direction were controlled via a custom-made software.

In total, 832 mg catalyst in 1040 mL isopropanol (0.8 mg mL<sup>-1</sup>) were spray-coated in four layers yielding ~300 mg of catalyst on the glass plate (5 mg cm<sup>-2</sup>). The time needed for all layers was ~12.5 h.

Prior to every catalytic experiment, a pretreatment was performed to remove any remaining organic compounds from the catalyst surface. After the quartz glass plate had been coated with the photocatalyst, it was placed in the reactor, which was subsequently purged with N<sub>2</sub> (50 mL min<sup>-1</sup>) to ensure an O<sub>2</sub>-free atmosphere and heated to 100 °C. The dry gas feed was changed to humid N<sub>2</sub> (4.5 % water in N<sub>2</sub>), and the photocatalyst layer was illuminated for 18 h (UV, 52.9 mW cm<sup>-2</sup>). The CO<sub>2</sub> evolution during this process was recorded and the photocatalyst was considered clean when y<sub>CO2</sub> was < 5 ppm. The alternative pretreatment conditions and standard reaction conditions are summarized in Table S1.

To allow for a reliable distinction between thermal and photocatalytic activity, the thermal activity (light off) was monitored at least 30 min before and after each photocatalytic test. The photocatalytic reaction was started by switching on the UV LED array. The methanol conversion  $X_{MeOH}$ , carbon-based relative product selectivities  $S_p$  were calculated from the methanol effluent

molar flow  $\dot{n}_{MeOH}$ , the molar feed flow of methanol  $\dot{n}_{MeOH,0}$  and the effluent molar flow of the products  $\dot{n}_p$  according to Equations S3 and S4, respectively.

$$X_{MeOH} = \frac{\dot{n}_{MeOH,0} - \dot{n}_{MeOH}}{\dot{n}_{MeOH,0}} \quad (S3)$$

$$S_p = \frac{\dot{n}_p \cdot v_p}{\sum_i \dot{n}_{p,i} \cdot v_{p,i}} \quad (S4)$$

Table S1. Reaction conditions of photocatalytic methanol oxidation and pretreatments (A-C). The respective catalytic test (Reaction 1 – Reaction 4) subsequent to the pretreatment is given in the third column.

Pretreatment/reaction	Conditions	Catalytic reaction
Reaction 1 - 4, Standard conditions	100 °C, UV light (368 nm), 1.5 % MeOH and 4.5 % H <sub>2</sub> O in N <sub>2</sub>	-
Oxidative pretreatment (A)	100 °C, UV light (368 nm), 4.5 % H <sub>2</sub> O in N <sub>2</sub> , 18 h	Reaction 1 + 2
Harsh oxidative pretreatment (B)	125 °C, UV light (368 nm), 4.5 % H <sub>2</sub> O, 10 % O <sub>2</sub> in N <sub>2</sub> , ~18h	Reaction 4
Reductive pretreatment (C)	125 °C, no UV light, 2 % H <sub>2</sub> in N <sub>2</sub> , ~18h	Reaction 3

A flow chart of the set-up used for *in situ* DRIFTS measurements is shown in Figure S1. The volumetric gas flow of the carrier gas He (5.0,  $\geq 99.999\%$ , Air Liquide) was controlled by three MFCs (Bronkhorst EL-Flow) with maximum flow rates of  $50\text{ mL min}^{-1}$  (MFC 1) and  $20\text{ mL min}^{-1}$  (MFC 2 and MFC 3). The tubing consisted of 1/8" and 1/4" stainless steel tubes which were partly heated to  $100\text{ }^{\circ}\text{C}$  to prevent condensation of reactants and products.

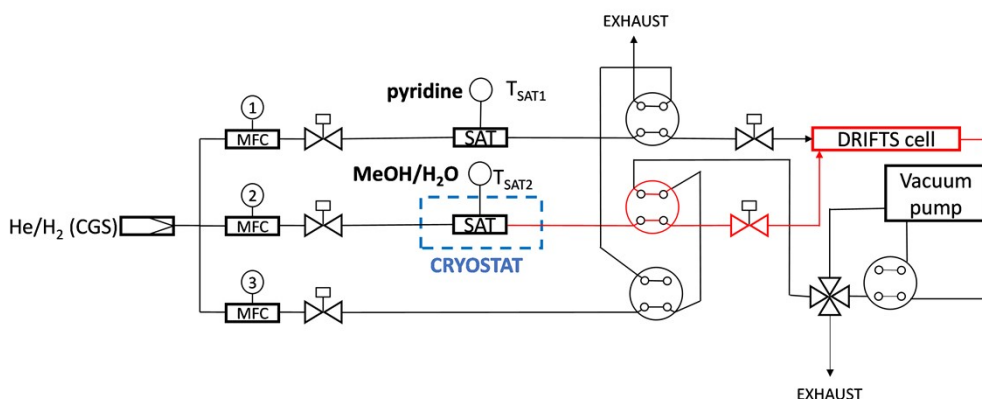


Figure S1. Flow chart of the set-up used for *in situ* DRIFTS measurements. Heated gas lines are marked in red ( $100\text{ }^{\circ}\text{C}$ ).

The temperature-controlled saturator enabled the dosing of methanol, water or mixtures of both components in the carrier gas according to the Antoine equation. The pyridine saturator was not used in this work. The samples were placed in a high-temperature reaction chamber (HTRC) made from stainless steel. The upper part included two IR-transparent ZnSe windows and one UV-transparent quartz window for photocatalytic experiments. It was removed to insert the sample into the sample holder on a steel mesh and was sealed by an O-ring and four screws. The gas entered the cell at one of the two inlets, passed the sample and left the cell through a pipe below the sample as visible in Figure S2. The HTRC was heatable up to  $450\text{ }^{\circ}\text{C}$  when used in He by a heating cartridge placed below the sample. Illumination of the sample was carried out by a 4x4 UV LED array (Lumitronix Nichia NCSU275 UV,  $10\text{ mm} \times 10\text{ mm}$ ,  $148\text{ mW}$  per LED,  $365\text{ nm}$ ) mounted on an aluminum heat sink with an electric fan for efficient cooling.

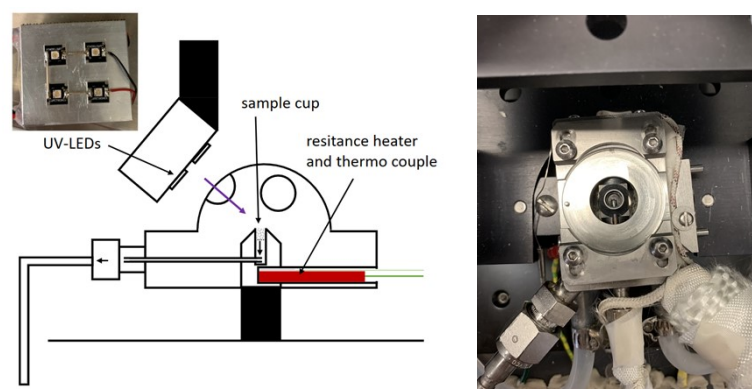


Figure S2. Scheme of the HTRC and UV-LEDs with gas flow direction and photograph of the LEDs as well as a photograph of the inside of the bottom part of the HTRC.

A FTIR spectrometer (Thermo Fischer Scientific Nicolet iS50) equipped with a KBr beam splitter, a Praying Mantis diffuse reflectance mirror geometry (Harrick), a LN<sub>2</sub> cooled MCT-A detector, and a DTGS detector was used. For DRIFTS measurements, the intensity of the DTGS detector was too low, therefore only the MCT-A detector was used due to the higher signal-to-noise ratio, shorter measurement time and higher spectral and temporal resolution. For all experiments, a resolution of 4 cm<sup>-1</sup> and 64 scans were applied. The spectrometer was constantly purged with water- and CO<sub>2</sub>-free air (PG28L, Peak Scientific) to avoid disturbances of the background spectra.

N<sub>2</sub> physisorption measurements (BET) were performed at a constant temperature of 77 K in a BELsorp-mini set-up. All samples were pretreated at 200 °C in vacuum.

XRD patterns of the samples were recorded in the 2θ range from 5 to 80° using a Bruker D8 Discover X-ray powder diffractometer. Cu Kα radiation with a wavelength of 0.154 nm was used and the analysis was performed with the Diffrac.Suite Eva software. Reference data (PDF-2 Release 2011) were obtained from the International Centre of Diffraction Data (ICDD).

Diffuse reflectance UV-Vis spectra were measured in the range of 600 – 200 nm with a data interval of 1 nm and integration time of 0.32 s per step. A Perkin Elmer Lambda 650 spectrometer with a praying mantis mirror geometry was used operated by the UV WinLab software. As 100 % reflectance standard, BaSO<sub>4</sub> (Sigma Aldrich, 97.5%) was used.

X-ray photoelectron spectroscopy (XPS) was performed with a Scienta Omicron HiPPLab system equipped with a HiPP-3 APPES analyzer and a high energy resolution monochromator with an Al Kα X-ray source. The spectra were obtained at a pass energy of 200 eV and a base pressure of 1 x 10<sup>-9</sup> mbar. The system is capable of measurements at near ambient pressures.

The Ti 2p<sub>3/2</sub> peak at 458.8 eV was used for calibration of the binding energies. The deconvolution of the spectra was performed using the CasaXPS software with Shirley-type background subtraction and symmetric and asymmetric Gaussian-Lorentzian line shapes. Based on the integrated peak areas, the surface composition was calculated using the corresponding sensitivity factors.

High-resolution and high angle annular dark-field scanning transmission electron microscopy (HR-TEM, HAADF-STEM), and energy dispersive X ray spectroscopy (EDX) were performed using a JEM-2200FS (JEOL, Akishima, Japan). For sample preparation, nanoparticles were dispersed in ethanol for 5 min by ultrasonic treatment, and the resulting dispersions were dropped on a carbon-coated copper grid.

Table S2. Results of catalyst characterization by means of ICP-OES (Pt content), TEM (average particle size), N<sub>2</sub> physisorption (specific surface area) and UV-Vis spectroscopy (band gap).

Nominal Pt loading / wt%	Pt content (ICP-OES) / wt%	Average Pt particle size (TEM) / nm	Specific surface area / m <sup>2</sup> g <sup>-1</sup>	Band gap (UV-Vis) / eV
0	0	-	24.0	3.11
0.1	0.09	2.6 ± 0.5	28.3	3.16

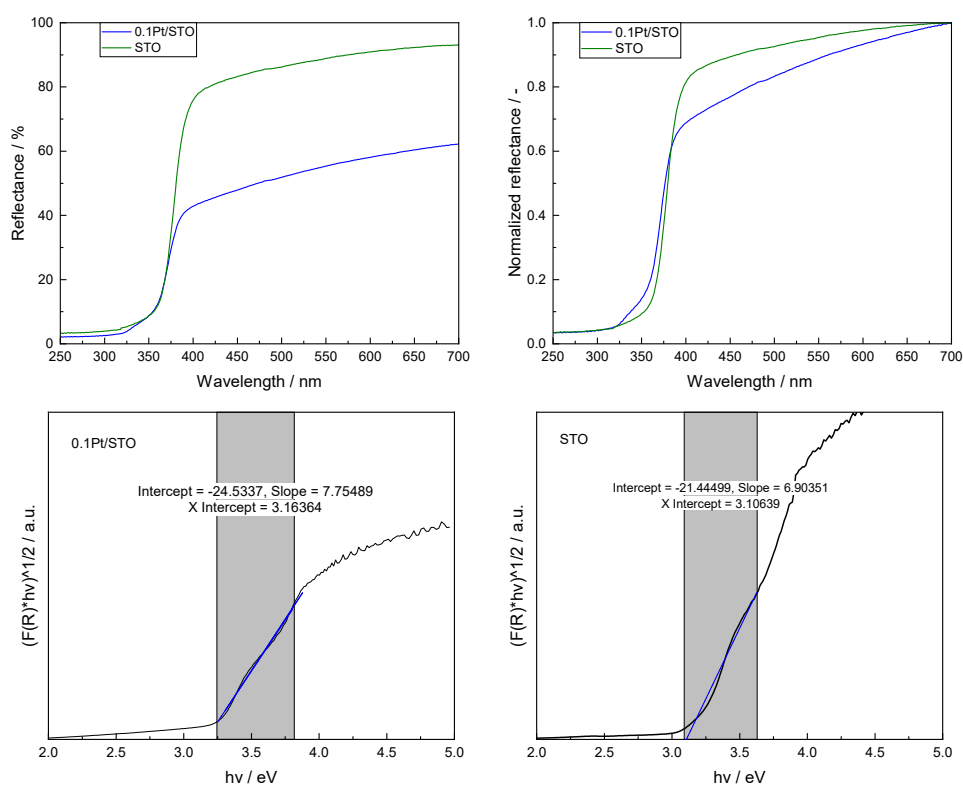


Figure S3. Diffuse Reflectance UV-Vis spectra (as measured and normalized) and Tauc plots of 0.1Pt/STO and STO.

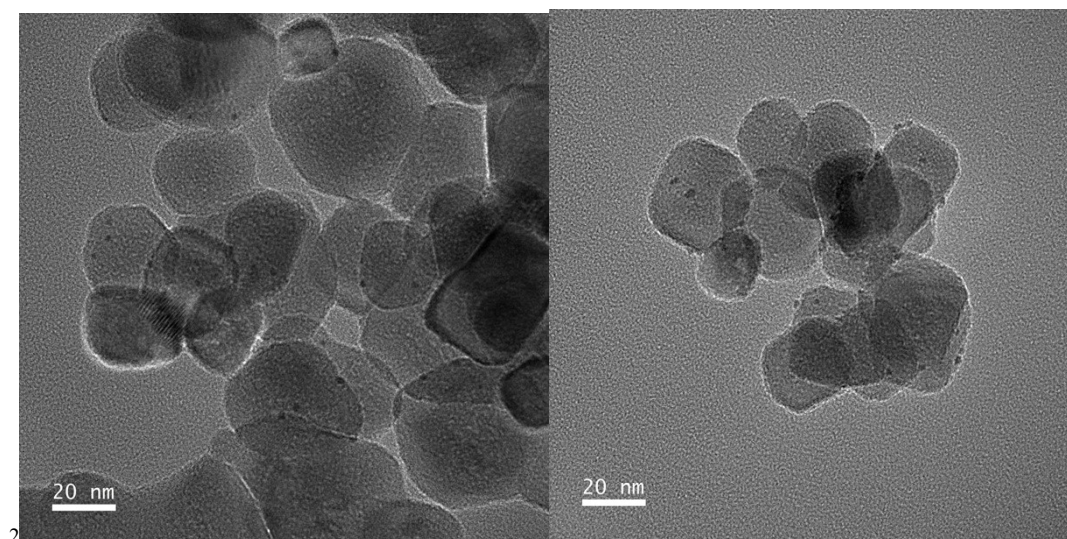


Figure S4. TEM images of 0.1PtSTO. Black spots display Pt nanoparticles on cubic STO particles.

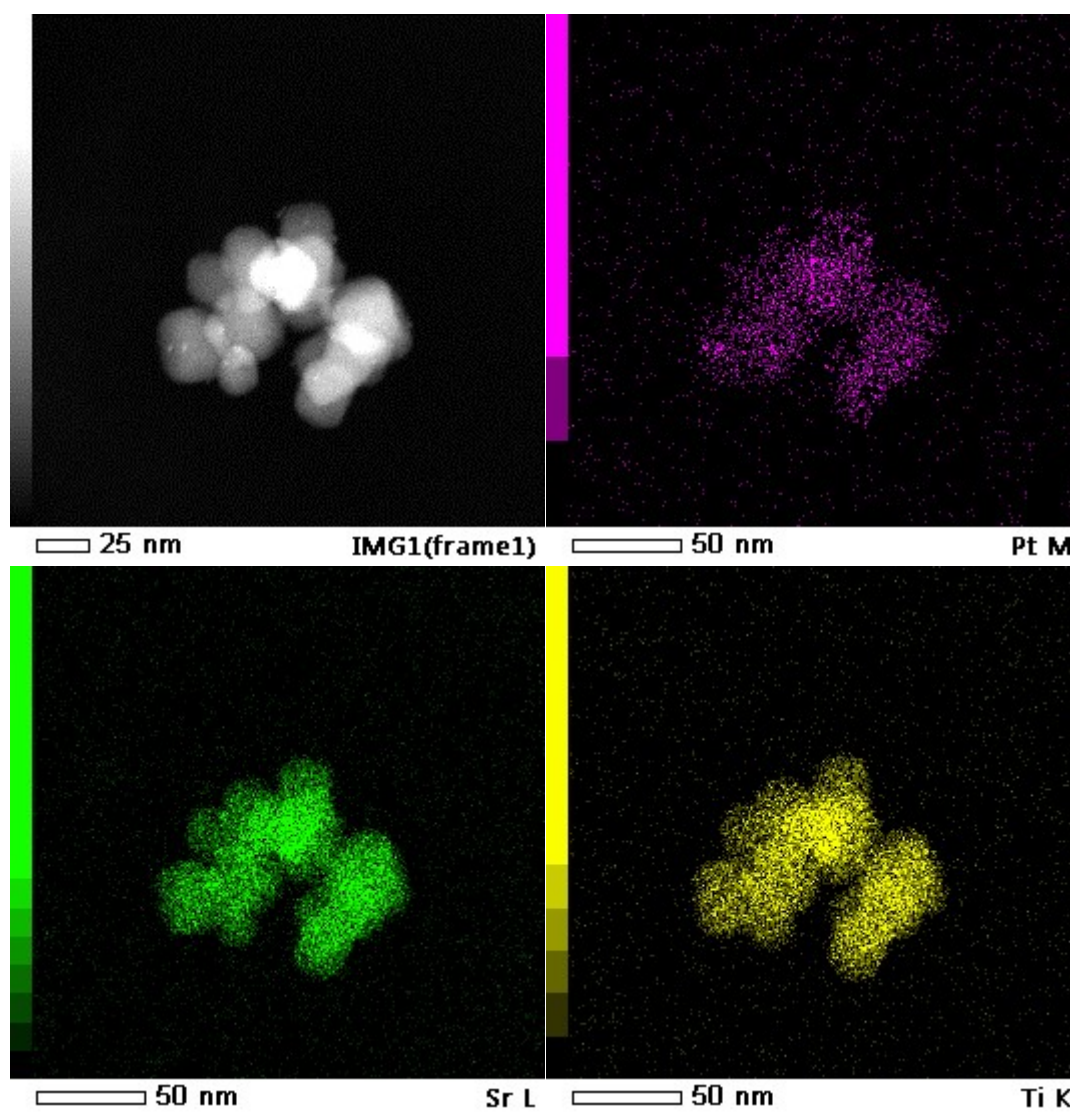


Figure S5. EDX elemental mapping of 0.1Pt/STO (Pt M, Sr L, Ti K).



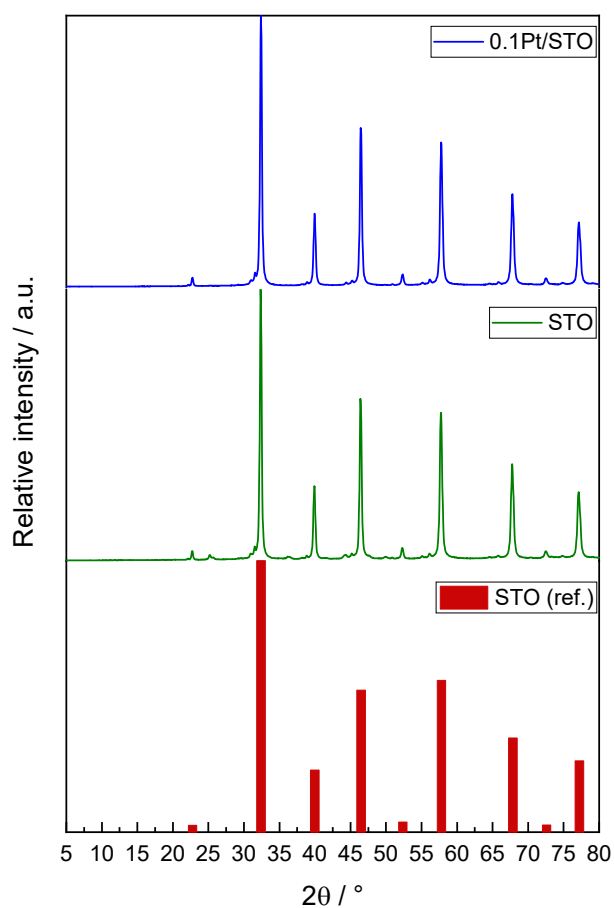


Figure S6. XRD patterns of 0.1Pt/STO and STO compared with a STO reference (PDF 00-005-0634).

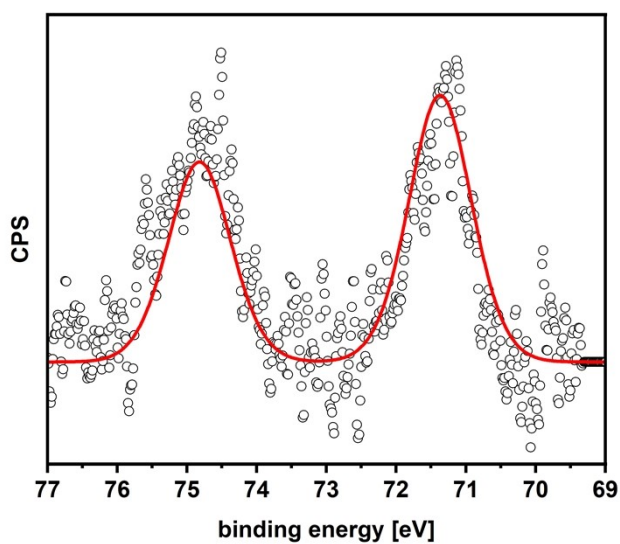


Figure S7. XP spectra (Pt 4f region) of 0.1Pt/STO. Peak fitting indicated the presence of Pt<sup>0</sup> as main species.

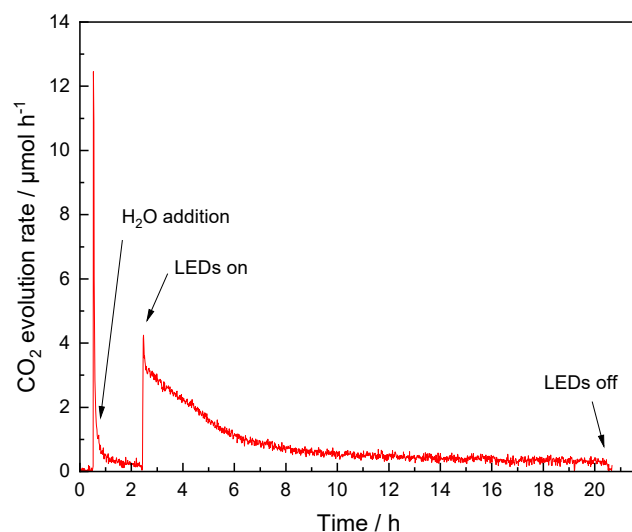


Figure S8. CO<sub>2</sub> evolution during the pretreatment cleaning procedure of 0.1Pt/STO by heating to 100 °C and subsequent UV-illumination in 4.5 % H<sub>2</sub>O in N<sub>2</sub> for 18 h.

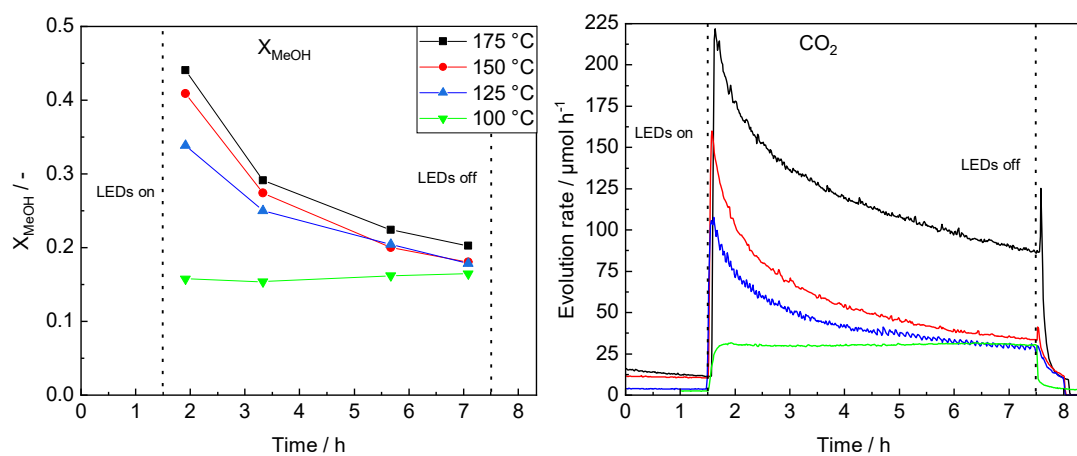


Figure S9. Temperature variation from 100 °C to 175 °C (single catalyst plates); temporal course of evolution rates of methanol conversion  $X_{MeOH}$  and CO<sub>2</sub> during UV illumination (Addition to Figure 1, Main part).



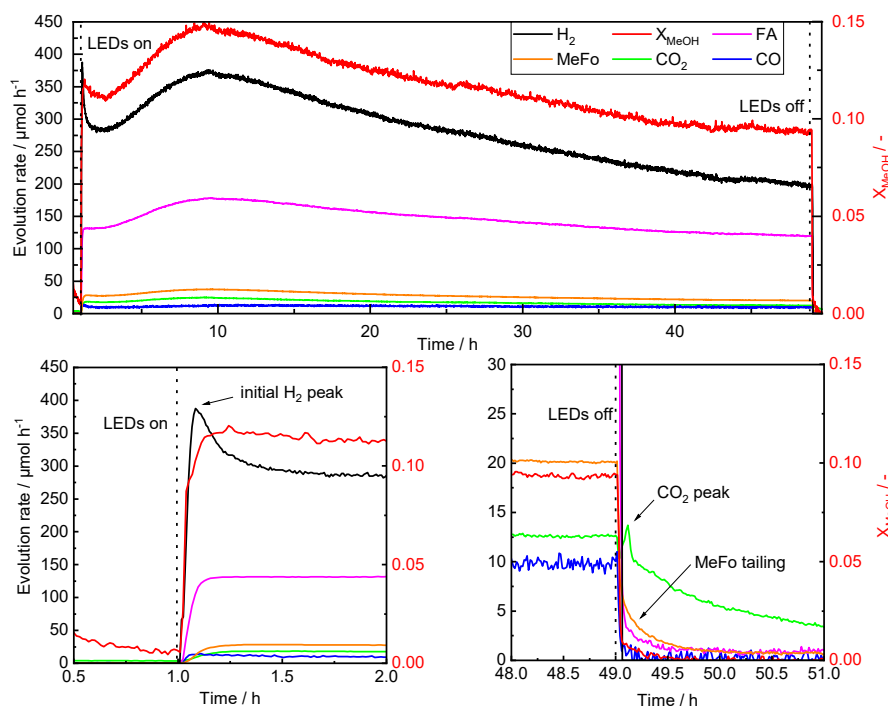


Figure S10. Gas evolution rates of  $\text{H}_2$ , formaldehyde, methyl formate,  $\text{CO}_2$ ,  $\text{CO}$  and methanol conversion  $X_{\text{MeOH}}$  during long-term photocatalytic test at standard conditions (top, equal to Reaction 2 in Figure S11). Initial excessive  $\text{H}_2$  evolution rate during methanol photooxidation over 0.1Pt/STO (bottom left) and enlarged end of the illumination period showing the tailing of the methyl formate evolution rate and  $\text{CO}_2$  peak (bottom right).

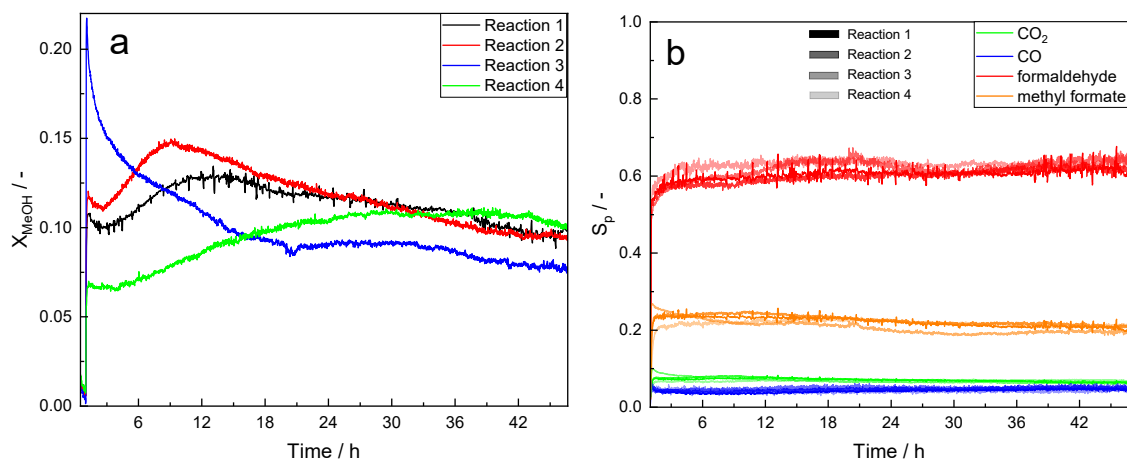


Figure S11.  $X_{\text{MeOH}}$  profiles (a) and profiles of selectivities to  $\text{CO}_2$ ,  $\text{CO}$ , formaldehyde and methyl formate (b) after oxidative or reductive pretreatment according to Table S1.

The influence of various pretreatments on the catalytic performance was studied in the following way: a catalyst layer was pretreated and applied in the photocatalytic methanol oxidation under standard conditions. Note that all pretreatments and catalytic tests were performed consecutively with the same catalyst layer according to the numbering in Table S1. Figure S11a shows the profiles of  $X_{\text{MeOH}}$  for each measurement. When reaching quasi steady-state conditions ( $> 48$  h

TOS),  $X_{MeOH}$  was at a similar level for all experiments, but the profiles for the initial part of the reaction differed substantially for the four measurements depending on the pretreatment. If only the standard oxidative pretreatment (A) was carried out,  $X_{MeOH}$  first increased followed by a steady deactivation over time. This was the case for Reactions 1 and 2 which received the same pretreatment. Before performing Reaction 3, a harsh oxidation treatment (B) was carried out to exclude organic residues on the catalyst. After that, a reductive pretreatment (C) was performed. This led to a high initial  $X_{MeOH}$  for Reaction 3 which was decreasing steadily. Before performing Reaction 4, only the harsh oxidation pretreatment (B) was performed. The following Reaction 4 showed a low initial  $X_{MeOH}$  which was slowly increasing with time. During all catalytic measurements, the product distribution remained similar (Figure S11b).

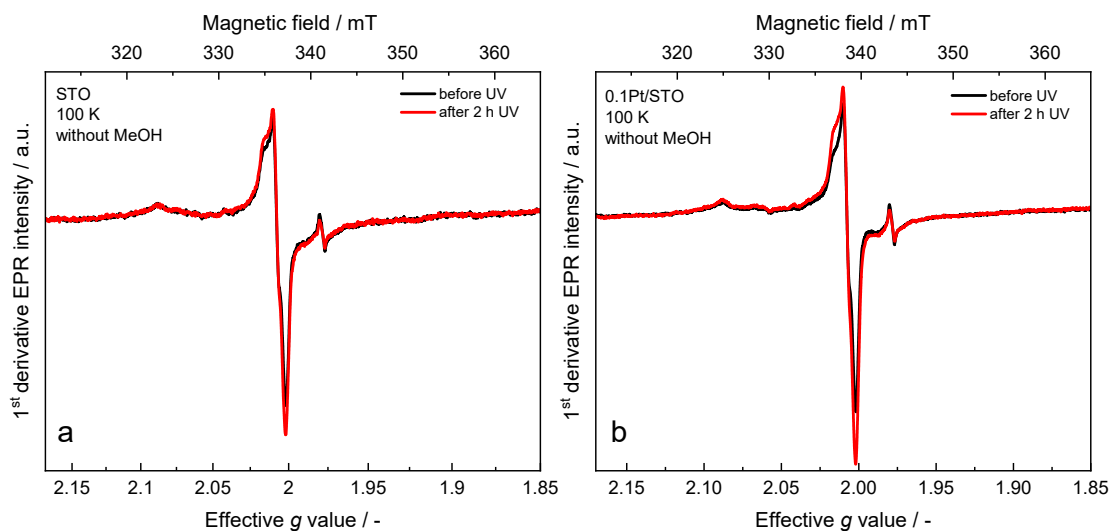


Figure S12. X-band CW EPR spectra of STO (a) and 0.1Pt/STO (b) in the absence of methanol at 2 hours UV illumination times.

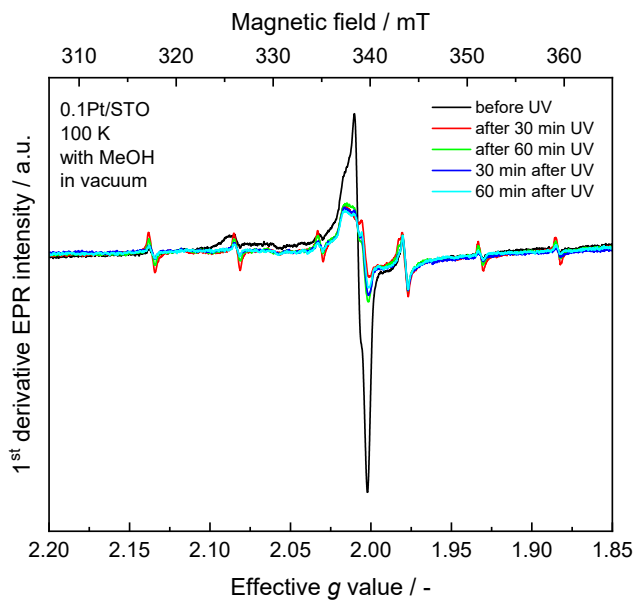


Figure S13. EPR spectra of 0.1Pt/STO with methanol and in vacuum after UV illumination and after storage at RT in the dark.

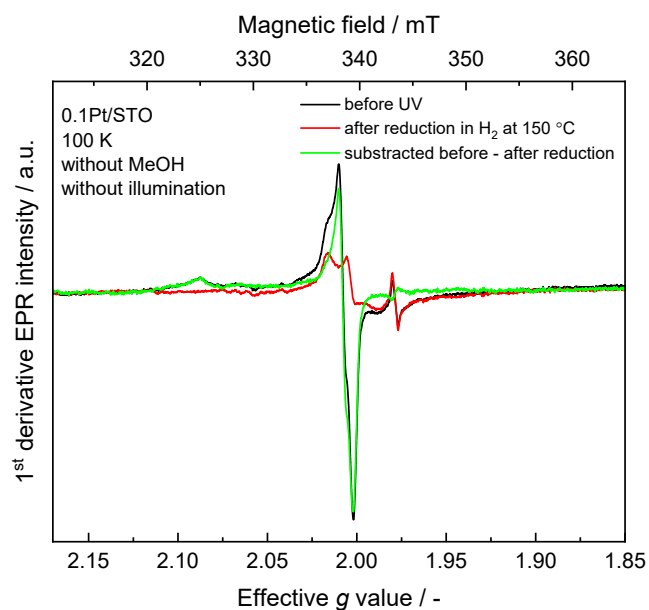


Figure S14. EPR spectra of 0.1Pt/STO without treatment and after reduction in H<sub>2</sub> at 150 °C. Subtraction of the two spectra reveals the line shape of the surface adsorbed  $O_{2[1-3]}^-$  with  $g_1 = 2.0021$ ,  $g_2 = 2.0085$  and  $g_3 = 2.0910$ .

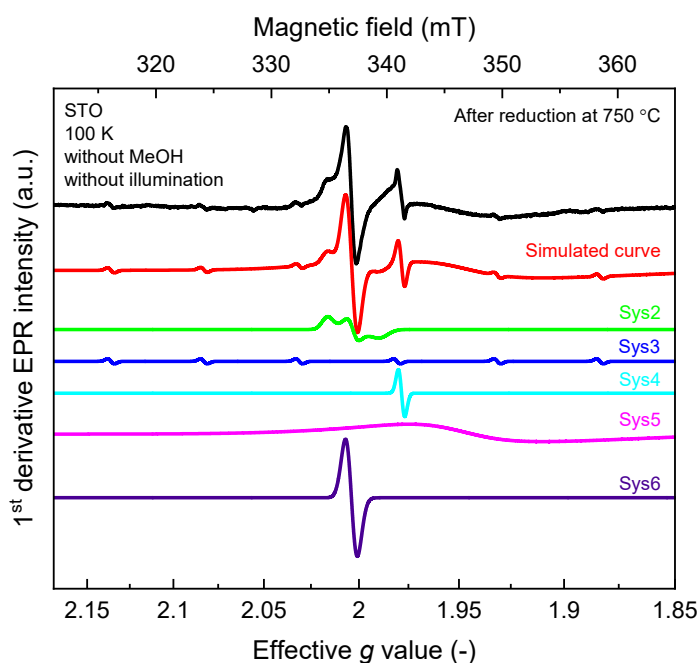


Figure S15. EPR spectrum of STO after reduction at 750 °C in 2 % H<sub>2</sub>/N<sub>2</sub> with a simulation assuming contributions from centres summarized in Table S3.

Table S3. EPR active sites identified in STO and Pt/STO materials.

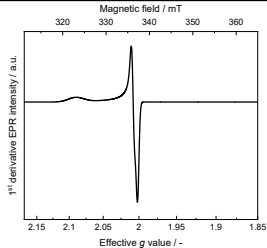
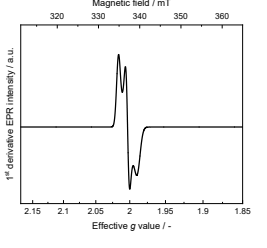
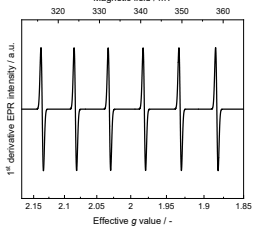
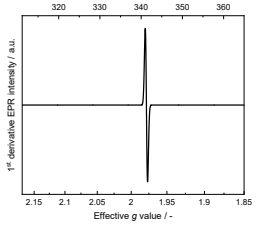
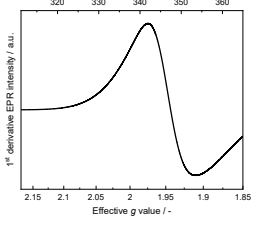
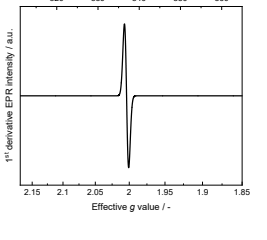
EPR spectrum	g-values	Line width ( $w$ ) Hyperfine ( $A$ )	Paramagnetic site															
	$g_1 = 2.0021$ $g_2 = 2.0085$ $g_3 = 2.0910$	$w = 20.7$ mT	Surface adsorbed $O_2^-$ [1-3]															
	$g_1 = 1.9889$ $g_2 = 2.0030$ $g_3 = 2.0164$	$w = 9.7$ mT	Hole trapping at the subsurface O site[4-6] in $TiO_2$ have very similar g-values and nature. This signal did not change during photocatalysis.															
	$g_{iso} = 2.0002$	$A_{Mn} = 237$ MHz	Mn replacing Ti <table border="1" data-bbox="860 896 1407 1064"><thead><tr><th><math>Mn_{Sr}^{2+}</math> /MHz</th><th><math>Mn_{Ti}^{4+}</math> /MHz</th><th><math>Mn_{Ti}^{2+}</math> /MHz</th><th><math>(Mn_{Ti}^{2+}-V_O)^0</math> /MHz</th><th>Ref.</th></tr></thead><tbody><tr><td>246</td><td>210</td><td>237</td><td>-</td><td>[7]</td></tr><tr><td>247</td><td>214</td><td>237</td><td>203</td><td>[8]</td></tr></tbody></table>	$Mn_{Sr}^{2+}$ /MHz	$Mn_{Ti}^{4+}$ /MHz	$Mn_{Ti}^{2+}$ /MHz	$(Mn_{Ti}^{2+}-V_O)^0$ /MHz	Ref.	246	210	237	-	[7]	247	214	237	203	[8]
$Mn_{Sr}^{2+}$ /MHz	$Mn_{Ti}^{4+}$ /MHz	$Mn_{Ti}^{2+}$ /MHz	$(Mn_{Ti}^{2+}-V_O)^0$ /MHz	Ref.														
246	210	237	-	[7]														
247	214	237	203	[8]														
	$g_{iso} = 1.9784$	$w = 4.1$ mT	$Ti^{3+}$ in the STO lattice[9,10]															
	$g_{\perp} = 1.95$ $g_{\parallel} = 1.93$	$w = 52-95$ mT	$Ti^{3+}$ in disordered STO phases[10,11]															
	$g_{iso} = 2.0039$	$w = 5.6$ mT	$Ti^{3+}/OV$ defects in STO[12]															

Table S4. Trace metal impurities in commercial STO (Sigma-Aldrich, 517011, Batch No. MKCQ8661) according to analysis certificate.

Metal impurity	Concentration / ppm
Total	$\leq 11315.7$
Aluminum (Al)	14.0
Barium (Ba)	900.0
Calcium (Ca)	10000.0
Chromium (Cr)	1.4
Iron (Fe)	9.5
Potassium (K)	30.0
Magnesium (Mg)	6.5
Manganese (Mn)	0.8
Sodium (Na)	350.0
Nickel (Ni)	2.5
Zirconium (Zr)	1.0

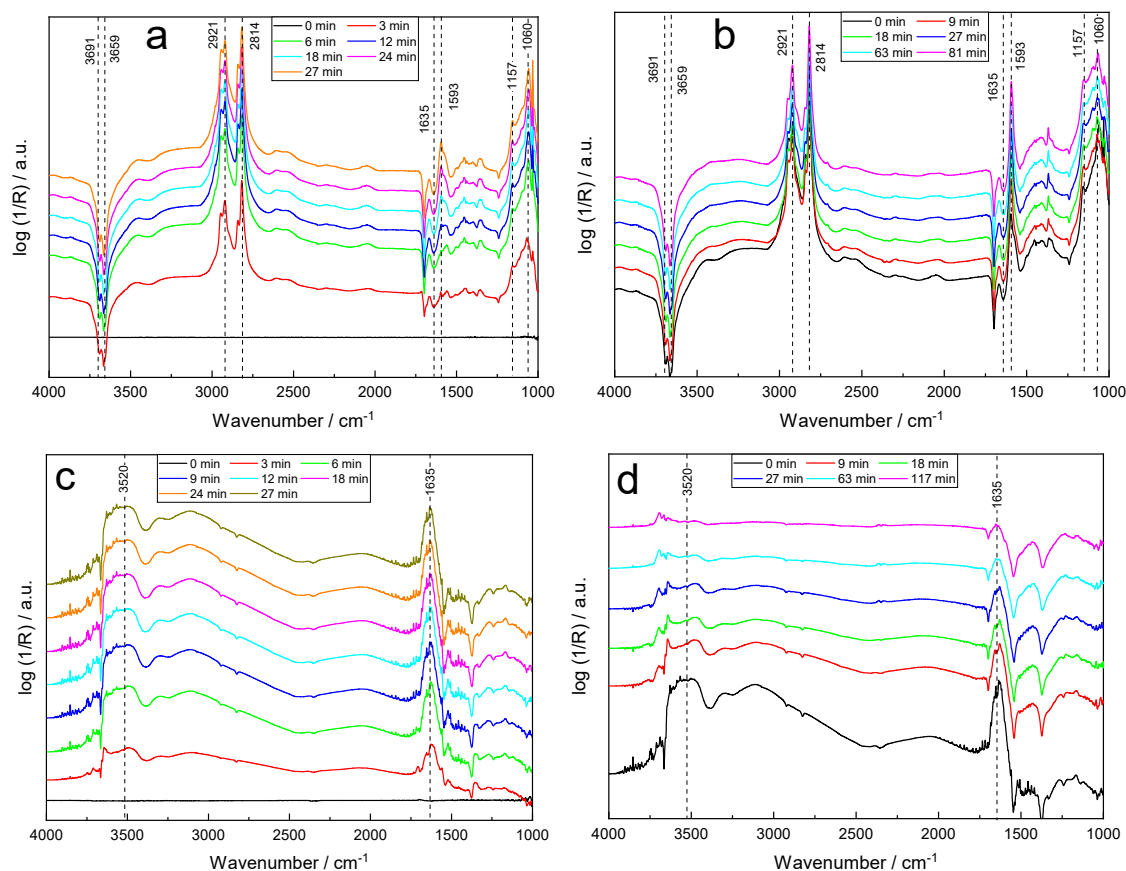


Figure S16. DRIFT spectra during adsorption of methanol (a) and water (c) and flushing with He at 100 °C (b and d) in the spectral region 1000 – 4000 cm<sup>-1</sup> for STO. As background spectra, the respective clean surface before contact to methanol and water at 100 °C was selected.

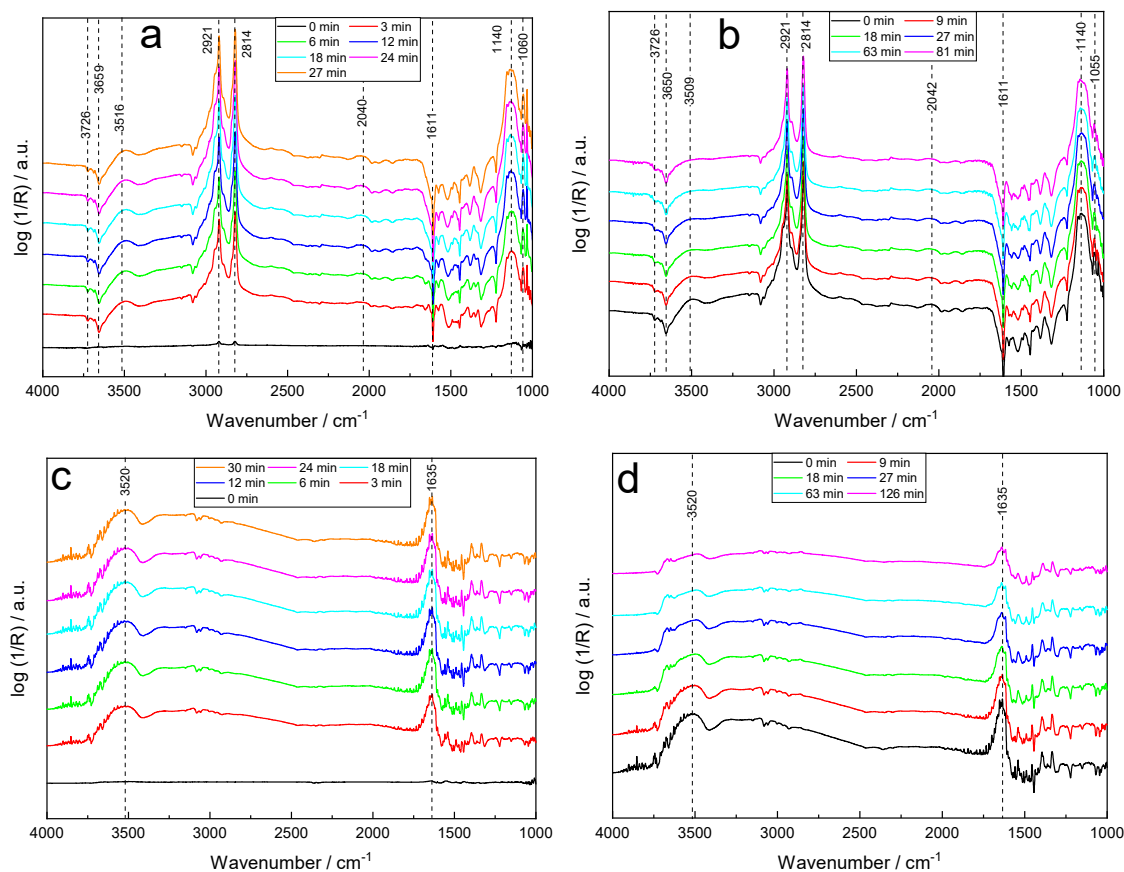


Figure S17. DRIFT spectra during adsorption of methanol (a) and water (c) and flushing with He at 100 °C (b and d) in the spectral region 1000 – 4000 cm<sup>-1</sup> for 0.1Pt/STO. As background spectra, the respective clean surface before contact to methanol and water at 100 °C was selected.



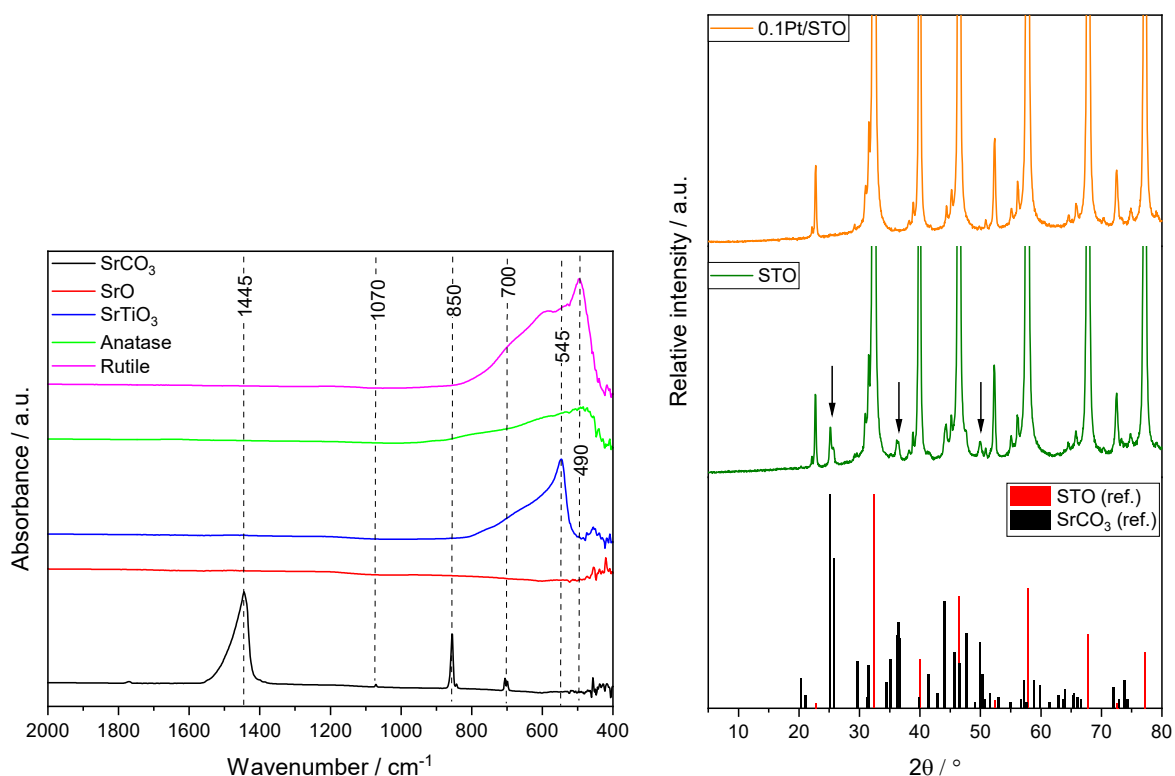


Figure S18. ATR-IR spectra of powdered  $\text{SrCO}_3$ ,  $\text{SrO}$ , STO and  $\text{TiO}_2$  (anatase and rutile) at room temperature (left) and XRD patterns of 0.1Pt/STO compared to pure STO before PD. Reflexes of  $\text{SrCO}_3$  are highlighted and compared to a  $\text{SrCO}_3$  reference PDF 00-005-0418 (right).

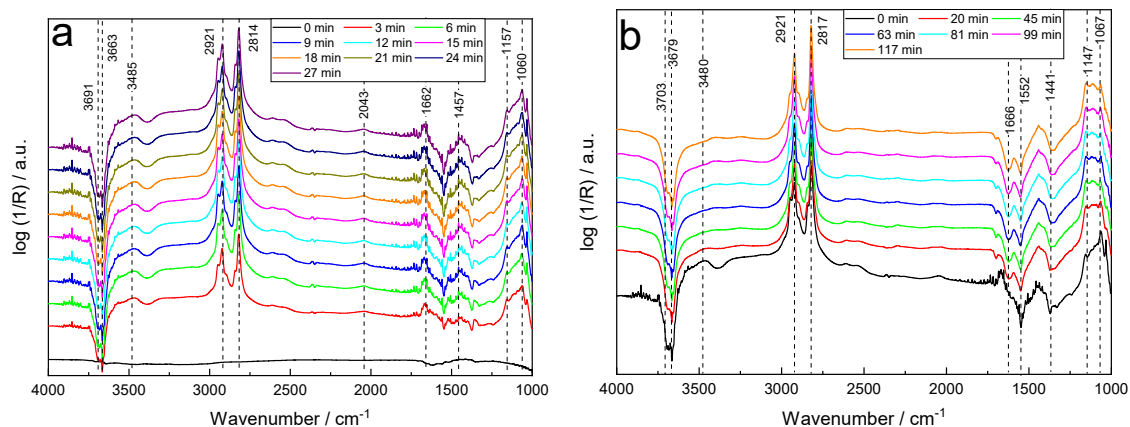


Figure S19. DRIFT spectra during adsorption of methanol and water and flushing with He at 100  $^\circ\text{C}$  in the spectral region 4000 – 1000  $\text{cm}^{-1}$  for STO (a: adsorption, b: He purging). As background spectra, the clean surface before the contact to methanol and water at 100  $^\circ\text{C}$  was selected.

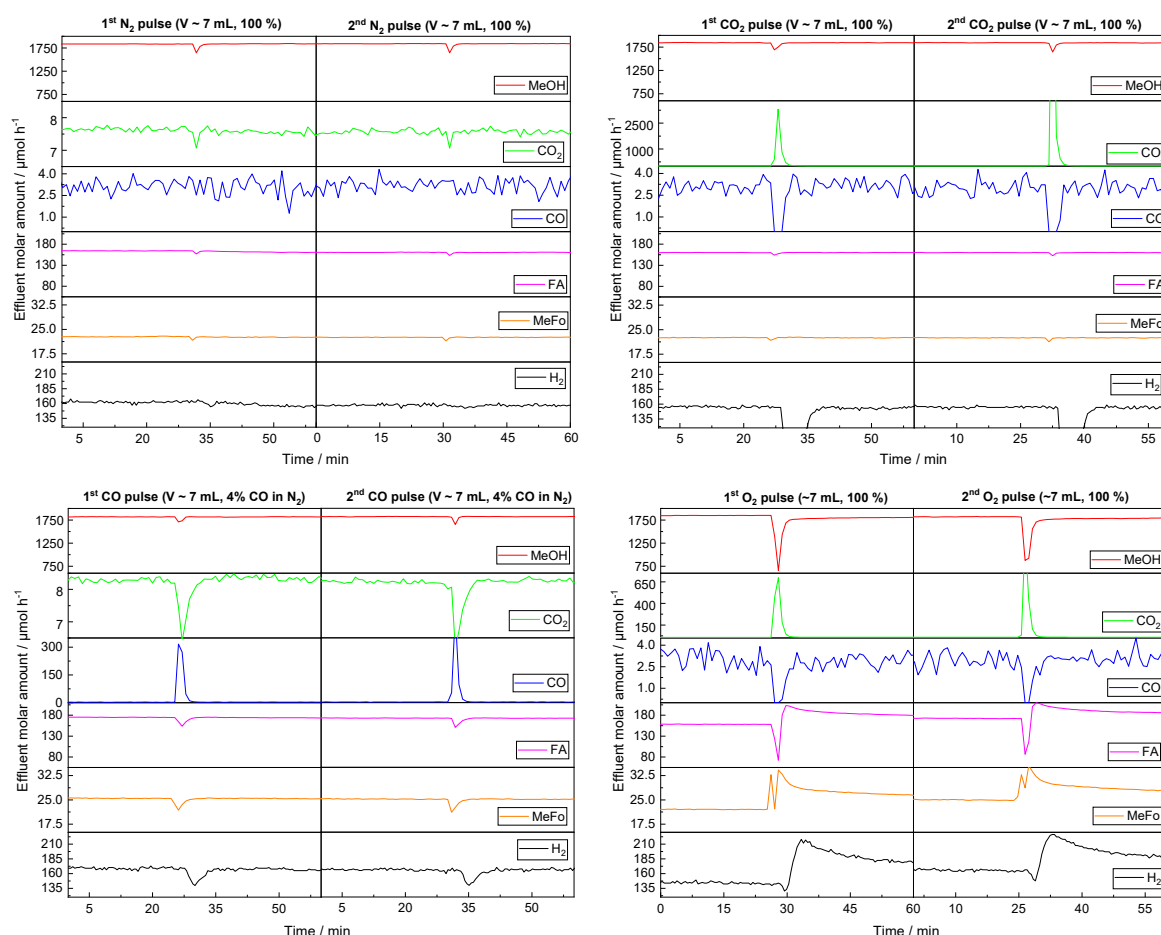


Figure S20. Effluent molar flow rates of methanol,  $\text{CO}_2$ , CO, formaldehyde methyl formate and  $\text{H}_2$  during pulses of  $\text{N}_2$  (dilution),  $\text{CO}_2$ , CO and  $\text{O}_2$ . Two consecutive pulses were carried out under quasi steady-state conditions.

The influence of  $\text{CO}_2$ , CO and  $\text{O}_2$  pulses on the photocatalytic performance under quasi steady-state conditions was studied (Figure S20). The temporal resolutions of the FTIR spectrometer and multichannel gas analyzer were 52 and 30 s, respectively. Thus, each pulse consisted of 6 – 7 data points which enabled only rough estimations using the pulse area so that mainly qualitative statements can be given.

The  $\text{N}_2$  pulse caused the temporary dilution of all components and was used as reference for the subsequent pulses.

To evaluate the possibility of  $\text{SrCO}_3$  formation,  $\text{CO}_2$  was pulsed to the reactant gas. Except the strongly increasing  $\text{CO}_2$  signal, only the  $\text{H}_2$  signal decreased more than during the dilution pulses, which was caused by cross-sensitivities in the TCD cell of the analytics and was reversed after the pulses. The missing response of the other compounds indicates that the formation of  $\text{SrCO}_3$  on the catalyst was unlikely or did not influence the catalytic performance.

Also, the CO pulses did not show significant differences compared to the dilution pulses.

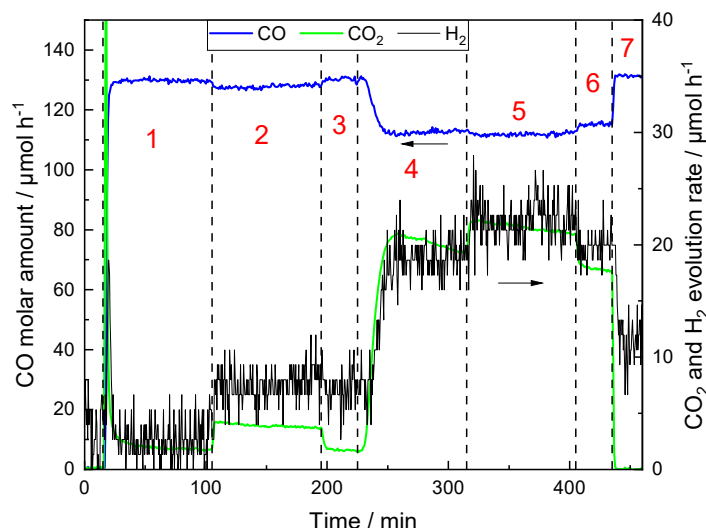


Figure S21. CO effluent molar amount and H<sub>2</sub> and CO<sub>2</sub> evolution rates during the WGS over 0.1Pt/STO. The reaction was performed at 100 °C under dark conditions (1 & 3) and UV illumination (2) and at 150 °C under dark conditions (4 & 6) and UV illumination (5). To calculate  $X_{CO}$ , the effluent CO molar amount was measured at RT in the dark (7).

To further address the influence of CO on the photocatalytic reaction, the ability of the catalyst to oxidatively remove CO (~900 ppm) with excess water vapor (~4.5 %) from the Pt surface was tested at 100 °C and 150 °C under dark and UV-illuminated conditions (Figure S21). The H<sub>2</sub>/CO<sub>2</sub> ratio during the experiment was ~1 indicating that the WGS is the only source of CO<sub>2</sub>.

At 100 °C,  $X_{CO}$  in the dark (1) and during UV illumination (2) were 1.4 % and 2.6 %, respectively. After increasing the reactor temperature to 150 °C,  $X_{CO}$  was 14.1 % in the dark (4) and only slightly increased to 14.9 % upon UV illumination (5).

Several studies showed that the ability of noble metal-containing catalysts to remove CO via the WGS depends on the type of metal and the reaction temperature. Colón et al. studied the synergy between photocatalytic and thermally catalyzed gas-phase methanol oxidation over Cu/TiO<sub>2</sub><sup>[13]</sup> and CuPd/TiO<sub>2</sub><sup>[14]</sup> and compared the results to a Pd/TiO<sub>2</sub> catalyst. In case of Pd/TiO<sub>2</sub>, a significant amount of CO was formed during the reaction which was partially inhibited when the bimetallic CuPd/TiO<sub>2</sub> catalyst was used. By applying elevated temperatures (up to 300 °C), the H<sub>2</sub>/CO ratio decreased even more. However, in case of Cu/TiO<sub>2</sub>, the formation of CO was hindered with increasing temperature due to the efficient WGS over Cu which is also used in industry as low-temperature WGS catalyst.<sup>[15]</sup> Bingham and Mills<sup>[16]</sup> studied the photocatalytic WGS over M/TiO<sub>2</sub> (M = Au, Pt, Pd, Ag). They found that Au was the most active cocatalyst for both the thermal and photocatalytic reaction. The highest photocatalytic activity was achieved at a temperature of 125 °C using a metal loading of 0.2 wt%, whereas the thermal activity scaled with temperature and metal loading.

- [1] M. Anpo, M. Che, B. Fubini, E. Garrone, E. Giamello, M. C. Paganini, *Top. Catal.*, 1999, 189–198.
- [2] S. M. Prokes, J. L. Gole, X. Chen, C. Burda, W. E. Carlos, *Adv. Funct. Mater.*, 2005, **15**, 161–167.
- [3] V. N. Belevskii, I. Volnov, S. A. Tokareva, *Consultants Bureau (Plenum Publishing Corporation)*, 1971, 1366–1367.
- [4] E. G. Panarelli, S. Livraghi, S. Maurelli, V. Polliotto, M. Chiesa, E. Giamello, *J. Photochem. Photobiol., A*, 2016, **322-323**, 27–34.
- [5] R. F. Howe, M. Grätzel, *J. Phys. Chem.*, 1987, **91**, 3906–3909.
- [6] C. P. Kumar, N. O. Gopal, T. C. Wang, M.-S. Wong, S. C. Ke, *J. Phys. Chem. B*, 2006, **110**, 5223–5229.
- [7] R. A. Maier, A. C. Johnston-Peck, M. P. Donohue, *Adv. Funct. Mater.*, 2016, **26**, 8325–8333.
- [8] R. A. Maier, E. Cockayne, M. Donohue, G. Cibir, I. Levin, *Chem. Mater.*, 2020, **32**, 4651–4662.
- [9] X. Zhang, Z. Li, B. Zeng, C. Li, H. Han, *J. Energy Chem.*, 2022, **70**, 388–393.
- [10] Russell F. Howe/Michael Gratzel, *J. Phys. Chem.*, 1985, **89**, 4495–4499.
- [11] M. Chiesa, M. C. Paganini, S. Livraghi, E. Giamello, *Phys. Chem. Chem. Phys.*, 2013, **15**, 9435–9447.
- [12] X. Zhou, N. Liu, T. Yokosawa, A. Osvet, M. E. Miehl, K. Meyer, E. Spiecker, P. Schmuki, *ACS Appl. Mater. Interfaces*, 2018, **10**, 29532.
- [13] F. Platero, A. López-Martín, A. Caballero, G. Colón, *ChemCatChem*, 2021, **13**, 3878–3888.
- [14] A. López-Martín, F. Platero, A. Caballero, G. Colón, *ChemPhotoChem*, 2020, **4**, 630–637.
- [15] R.-R. Lee, I.-J. Jeon, W.-J. Jang, H.-S. Roh, J.-O. Shim, *Catal.*, 2023, **13**, 710.
- [16] M. Bingham, A. Mills, *J. Photochem. Photobiol., A*, 2021, **409**, 113133.